



Build Optimization for Selective Laser Melting of 316L Stainless Steel and Parameterization for Cross-Material Comparison and Process Design

R.E. Napolitano, S. Jain, C. Sobczak, B.A. Augustine, and E.M. Johnson

Submitted: 3 January 2021 / Revised: 14 April 2021 / Accepted: 1 May 2021 / Published online: 17 May 2021

Optimization of selective laser melting process parameters with respect to microstructure and mechanical properties is examined for 316L stainless steel. Strength, ductility, and hardness are found to scale with power ratio, a proposed normalized melting intensity parameter accounting for the combined effects of process variables and material properties. Sound-build limits and the existence of an optimum power ratio are established. Poor properties at low power ratio are attributed to insufficient fusion, while property degradation above the optimum is correlated with increases in grain size and grain boundary defect frequency. Single-trace measurements are used to correlate power ratio with melt-pool cross-section dimensions, which are further shown to scale with curvature at the root of the melt pool, providing a direct bulk-build measure of the melting intensity. With strong correlation to the melt pool size, soundness of fusion, porosity, grain boundary defects, and mechanical properties, the utility of the power ratio as a design parameter is examined. By coupling the power ratio with a linear process rate and/or a dimensionless thermal dissipation time, sound-build process maps are used to assess reported data for several alloy systems, further demonstrating the value of the proposed parameterization as cross-material platform for process design.

Keywords additive manufacturing, power ratio, process mapping, selective laser melting

1. Introduction

As the benefits associated with design flexibility and local microstructure control afforded by additive manufacturing processes continue to expand, so too does the range of potential applications and alloys. Indeed, powder-bed laser fusion methods, such as selective laser melting (SLM), have seen increased production-based implementation and show great promise as additive methods for producing net shape components with desirable properties over a broad range of alloys and components (Ref 1-6). Even so, many questions remain unresolved in fundamental areas such as laser-material interactions, heat transfer, fluid dynamics, melting, vaporization, and solidification (Ref 1, 2). These are central to practical issues of integrated process/component design addressing laser scan strategy and component geometry with the goal of controlling microstructure and physical properties.

This invited article is part of a special topical focus in the Journal of Materials Engineering and Performance on Additive Manufacturing. The issue was organized by Dr. William Frazier, Pilgrim Consulting, LLC; Mr. Rick Russell, NASA; Dr. Yan Lu, NIST; Dr. Brandon D. Ribic, America Makes; and Caroline Vail, NSWC Carderock.

R.E. Napolitano, S. Jain, and C. Sobczak, Department of Materials Science and Engineering, Iowa State University, Ames, Iowa; and **B.A. Augustine and E.M. Johnson**, John Deere and Company Moline Technology Center, Moline, Illinois. Contact e-mail: ren1@iastate.edu.

The overall process is inherently complex with many physical phenomena operating simultaneously over several length scales. In some sense, it is useful to view the overall problem as three coupled scenarios. These include: (i) the localized direct heating response in the immediate vicinity of the laser and melt pool, (ii) the micro-/meso-scale effects of heat transfer, melting, and solidification associated with a single laser-melt trace, and (iii) the long-range influence of multiple laser-trace passes, where local and non-local heating, repetitive melting and re-solidification are influenced by the layer-by-layer build strategy in conjunction with the overall component geometry. High sensitivities to the related process and material parameters further complicate matters, where the degrees of freedom and corresponding variability in microstructure become virtually unbounded. Indeed, with many outstanding questions across these areas, prediction and control of microstructures and properties attainable through SLM processing are the subjects of numerous recent and current studies (Ref 1).

Systematic investigation aimed at correlating process conditions with as-built microstructure and properties is necessary for enhanced SLM capability, but variation over the broad range of process and material parameters can limit the utility of direct comparison. Even so, there is a great need for general guidance relating SLM build strategy with material properties as a design tool. Of course, the basic process variables of laser power and scan velocity/pattern are central to such work, with a common objective being outcome-based maps of process-parameter space, which (i) define the sound-build regimes, (ii) identify the physical origin of the limiting boundaries, (iii) quantify the microstructure/property sensitivities within these boundaries, and (iv) provide a framework to identify optimal conditions within the sound-build regime, depending on design objectives. To this end, parametric studies have been reported

for a variety of alloy systems, including Al-, Cu-, Fe-, Ni-, and Ti-based alloys. (See, for example, Refs. (Ref 7-12, 12-46), and (Ref 47-57), respectively.) These provide useful information for specific alloys, but, without common or normalized parameter spaces over which to construct a unified process map for SLM, their broad utility toward these purposes cannot be fully realized.

Quantification of process conditions is centered around the amount of energy imparted by the laser to the process volume. Accordingly, the volumetric energy density, defined as $E_D = P_n / v\lambda h$, where P_n is net laser power, v is scan speed, λ is layer thickness, and h is hatch spacing, is generally accepted as a fundamental characteristic descriptor of process conditions, although limitations have been identified (Ref 58, 59). Areal (2D) and linear (1D) analogs of volumetric energy density have also been used (Ref 60, 61).

Likewise, the thermal field associated with a single trace can be reasonably well characterized by analytical treatments, such as the Rosenthal model (Ref 62), which describes the temperature distribution associated with a point source moving at a fixed velocity, accounting for local heating and dissipation through the substrate (by conduction only) but not accounting for the latent heat of melting or surface heat losses. Simulation-based treatments of melt-pool shape within multi-trace builds have further shown the correlation of melt-intensity and melt-pool shape with insufficient fusion (Ref 63) and other microstructural features (Ref 64). Beyond single-trace heating and reheating effects, non-local preheating effects associated with neighboring laser traces and repetitive melting/freezing can be predicted for a given scan pattern and inter-pass dwell time (i.e., reciprocal of scan frequency) (Ref 65). These treatments can be used to describe typical local thermal history within a build and the spatial variation of such profiles, but the lack of an effective parameterization for meaningful build-to-build comparisons across different alloys and geometries remains as a limiting factor in comparative parametric evaluation and design of SLM processes.

The work presented here is principally aimed at systematic assessment of the build parameter space for 316L stainless steel manufactured by SLM, but the results are offered within the broader context of a unified cross-material parameter space. Many parametric studies of SLM processing of this alloy have been reported (Ref 12, 23, 25-29, 33-35, 37, 66-72), as summarized in Table 1. To provide additional clarity related to process parameter sensitivity and to establish sound-build limits, a large range of processing conditions is explored here using simple build geometries and a combination of microstructural and mechanical analyses. As a framework for our investigation, we introduce a parameterization that couples a dimensionless material-normalized local melting intensity with a rate-dependent linear power density. Using this parameter space, melting characteristics, microstructure, and mechanical properties are examined for 316L test builds to suggest operational limits and optimal process parameters for the SLM process. Comparisons with reported data for several alloy systems are made to demonstrate the value of the proposed parameterization as cross-material platform for process design. In addition, we use a dimensionless thermal relaxation time to characterize the normalized thermal dissipation behavior of the material. Comparing reported build outcomes for Al-, Fe-, Ni-, and Ti-based alloys, we show the utility of this parameterization for general cross-material SLM process mapping.

2. Experiments

Four specific types of SLM test specimens were fabricated* using a range of build parameters. Specimen types include (a) cube-shaped specimens with a 10-mm edge dimension, (b) single-trace builds involving one powder layer and an isolated one-pass laser trace, (c) double-layer builds including two full powder layers deposited using a bulk build scan pattern, and (d) cylindrical pillar-type builds from which tension test specimens were fabricated. Multilayer builds (a, c, d) were fabricated using a serpentine raster pattern in the powder-spread scan (x - y) plane with a 60-degree rotational offset (about the z -axis scan plane normal) applied between successive layers so that there are three distinct principal trace directions in each bulk specimen. An example of a typical as-built structure in a bulk specimen (i.e., cube and pillar) is shown in Fig. 1, revealing the melt-trace pattern and microstructure on three section planes.

To probe and identify the sound-build limits with respect to processing conditions and to investigate the variation of structure and properties within and beyond those limits, a range of values for laser power (P) and scan velocity (V) were employed, as listed in Table 2. All test builds were produced with a 316L powder** (20-53 μm diameter), using a spread layer depth increment of 0.040 mm and a hatch spacing (between successive parallel traces in a scan pattern) of 0.100 mm.

For each set of build parameters, pore area fraction was measured optically on polished (unetched) 2D sections of the cube-shaped samples. A total of 43 fields of view were used for each sample, including 20, 15, and 8 fields of view in the XY, XZ, and YZ planes, respectively, with each field of view representing a true spatial area of 3.53×2.67 mm resolved as 1288×972 pixels (2.75 μm resolution). As such, the method is very sensitive to coarse porosity, resulting from incomplete melting/fusion but generally insensitive to micron- or sub-micron-scale porosity. The results in Fig. 2(a) show that, as expected, porosity increases dramatically for decreasing P at constant V or increasing V at constant P . Moreover, abrupt change thresholds are indicated by both curves. In Fig. 2(b), the porosity measurements are plotted against a dimensionless local melting intensity parameter, defined here as

$$\phi = \frac{\alpha P}{r_m(c_p^S(T_m - T_A) + \Delta H_m + c_p^L \Delta T_S)} \quad (\text{Eq 1})$$

where all included physical quantities are given in Table 3. Using this parameter, termed here as the *power ratio*, the two curves collapse to a single behavior. This is not surprising, considering that ϕ is essentially the well-utilized *energy density* (Ref 73) normalized by the power requirements for heating *and melting* the given material at the prescribed process rate. The value of the ϕ parameter is better illustrated, however, when coupled with a complementary rate-sensitive *linear power density*, θ , defined here as PV/D , where D is the thermal diffusivity. Several pairs of structures with similar values of ϕ are compared in Fig. 2(c-g), showing not only that builds in each pair exhibit similar total porosity, but also that features such as pore size, number density, and pore shape appear to be virtually identical. This observation suggests that ϕ defines a

*Specimens were fabricated with an EOS M280 instrument.

**The 316L powder used in this investigation was produced by Hoganas North American.

Table 1 A summary of reported parametric investigations of SLM processing of 316 L stainless steel

| Laser power, W | Layer thickness, μm | Scan rate, mm/s | Hatch spacing, mm | Particle size ^a , μm | Beam dia ^b , μm | Energy density ^c , J/ mm^3 | Refs. |
|----------------|--------------------------------|-----------------|-------------------|---|---------------------------------------|--|-------|
| 250-500 | 100-250 | 40-110 | 0.15 | {42/75/155} {6/20/38} | 300 | [60.6-833] | [72] |
| 200 | 50 | NR | NR | [10-45] | NR | | [67] |
| 100 | 60 | 90-180 | 0.1 | (31.75) | NR | [92.6-185] | [70] |
| 60-200 | 50-100 | 20-300 | 0.1-0.8 | {3/20/40} {6/30/50} | NR | [2.5-2000] | [69] |
| 104 | 30, 45 | 175-800 | 0.13 | {7.12/15.12/24.17} {19.84/28.26/41.13} {15.26/37.7/55.54} | NR | [22.2-152] | [28] |
| 80-100 | 50-100 | 100-300 | 0.08 | <27>, (47) | NR | [41.7-250] | [66] |
| 100-200 | 100 | 40-200 | NR | [15-20] | 300-500 | | [23] |
| 100-400 | 50 | 50-4000 | NR | NR | (52, 130) | | [35] |
| 150-400 | 30 | 500-1800 | NR | NR | 30, (54) | | [34] |
| 200 | NR | 2000 | NR | NR | (54) | | [71] |
| 37.5-82.5 | 25 | 200-500 | NR | [5-50] | 20 | | [12] |
| 50-200 | 40 | 50-600 | 0.08 | {22.5/39.02/56.04} {46.2/108.06/174.48} | 70 | [26-1250] | [68] |
| 100-150 | NR | 700 | 0.07 | [15-45] | 50 | | [25] |
| 80-100 | 60-80 | 570-2100 | 0.02 | <35> | NR | [23.8-109.7] | [29] |
| 150-225 | 50 | 100-1200 | 0.03 | {15/32/45} | NR | 83-1333 | [26] |
| 25-100 | 20 | 700-1700 | 0.04-0.12 | {15/35.5/55} | NR | 22.3-333.3 | [33] |
| 400 | 250 | 50-125 | 0.24-0.3 | {5/18/41} | NR | [42.6-133.3] | [27] |
| 185-215 | 30 | 900-1000 | 0.1 | {15.97/21.92/32.74} | NR | 83.6-110.7 | [24] |
| 100 | 50 | 111-239 | 0.111-0.12 | {30.24/40.80/56.25} | 200 | 70-150 | [37] |

^aWhere three numbers are listed, values reflect {D10/D50/D90} sizes. Where two numbers are listed, values reflect reported [min-max] sizes. Single values indicate an < avg > size or a (max) size corresponding to a reported screen mesh. NR denotes Not Reported.

^bEntries differentiated by () give the reported D4 σ value. Others are unspecified beam diameters.

^cEntries differentiated by [] give the calculated energy density range, while others are as reported.

**Fig. 1** A typical bulk-build structure, viewed on three section planes. The top surface is normal to the beam (z axis) and parallel to the scan (x - y) plane. Laser scan directions within the scan plane include the direction normal to the front face along with 60 and 120 degree rotations about the z axis from the front face normal.**Table 2** SLM specimen build parameters

| Specimen | V , mm/s | P , W | ϕ | θ , kW-m/s |
|----------|------------|---------|--------|-------------------|
| A | 2832 | 200 | 0.97 | 34.71 |
| B | 2000 | 200 | 1.37 | 24.51 |
| C | 1416 | 200 | 1.93 | 17.35 |
| D | 1132 | 200 | 2.42 | 13.87 |
| E | 944 | 200 | 2.90 | 11.57 |
| F | 810 | 200 | 3.38 | 9.93 |
| G | 708 | 200 | 3.87 | 8.68 |
| H | 630 | 200 | 4.35 | 7.72 |
| I | 566 | 200 | 4.84 | 6.94 |
| J | 944 | 67 | 0.97 | 3.88 |
| K | 944 | 100 | 1.45 | 5.78 |
| L | 944 | 133 | 1.93 | 7.69 |
| M | 944 | 167 | 2.42 | 9.66 |
| N | 944 | 200 | 2.90 | 11.57 |
| P | 944 | 233 | 3.38 | 13.48 |
| Q | 944 | 267 | 3.87 | 15.44 |
| R | 944 | 300 | 4.35 | 17.35 |
| S | 944 | 333 | 4.83 | 19.26 |
| T | 1250 | 275 | 3.01 | 21.06 |
| U | 1500 | 250 | 2.28 | 22.98 |
| V | 1750 | 225 | 1.76 | 24.13 |

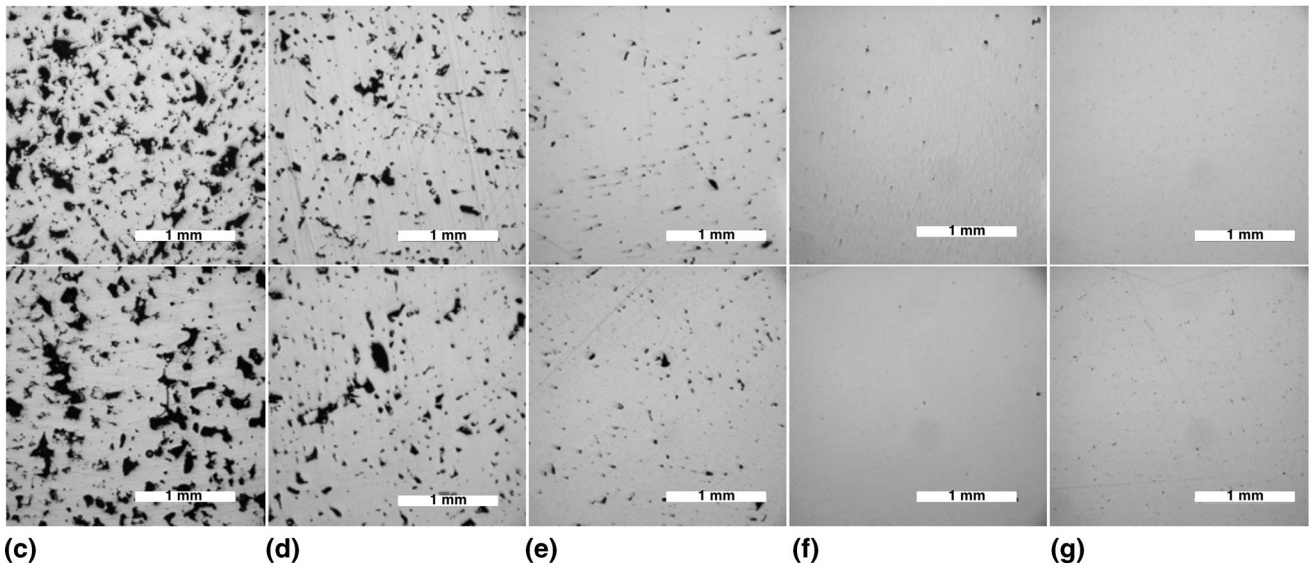
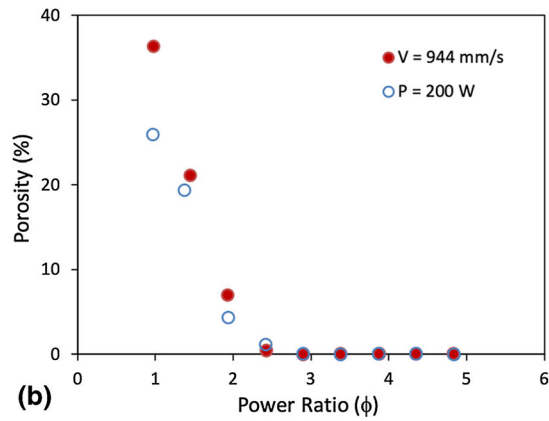
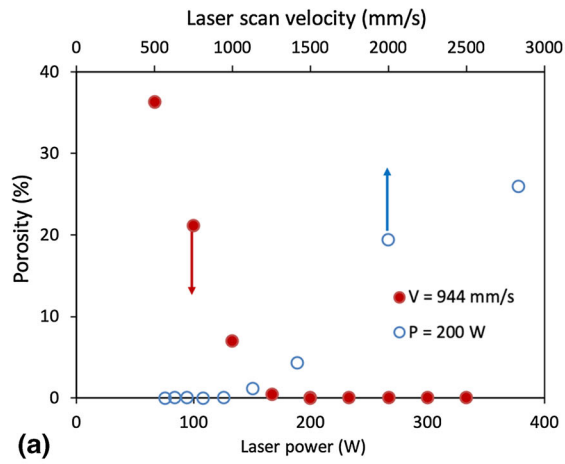


Fig. 2 Measured large-scale porosity, including (a) variation with P and V; (b) variation with the power ratio, ϕ ; and a comparison of selected test build pairs with similar ϕ [build letters given, see Table 2]; (c) $\phi \approx 1.5$ [B,K], (d) $\phi \approx 2$ [C,L], (e) $\phi \approx 2.6$ [M,D], (f) $\phi \approx 3.5$ [P,F], (g) $\phi \approx 4.3$ [R,H]

Table 3 Process and material parameters

| Parameter | Description | Units | Value used here |
|--------------|------------------------------|--------------------|--------------------------------------|
| α | Absorption coef. | ... | 0.25 |
| c_p^S | Heat capacity (solid) | J/gK | 0.449 |
| c_p^L | Heat capacity (liquid) | J/gK | 0.537 |
| T_m | Melting temperature | K | 1672 |
| T_A | Ambient temperature | K | 298 |
| D | Thermal diffusivity | mm ² /s | 4.075 |
| ΔH_m | Latent heat of fusion | J/g | 247.3 |
| ΔT_S | Superheat | K | 0 |
| δ | Powder layer thickness | mm | 0.04 |
| λ | Hatch spacing | mm | 0.1 |
| d | Laser beam diameter | mm | 0.1 |
| ρ_a | Alloy density | g/cm ³ | 7.874 |
| ρ_p | Packing density | ... | 0.6 |
| r_m | Mass rate | g/s | ($\rho_a \rho_p \delta \lambda V$) |
| P | Laser power | W | See Table 2 |
| V | Laser scan speed | mm/s | See Table 2 |
| ϕ | Power ratio | ... | See Eq 1 |
| β | Geometric dissipation factor | ... | 0.0285 |

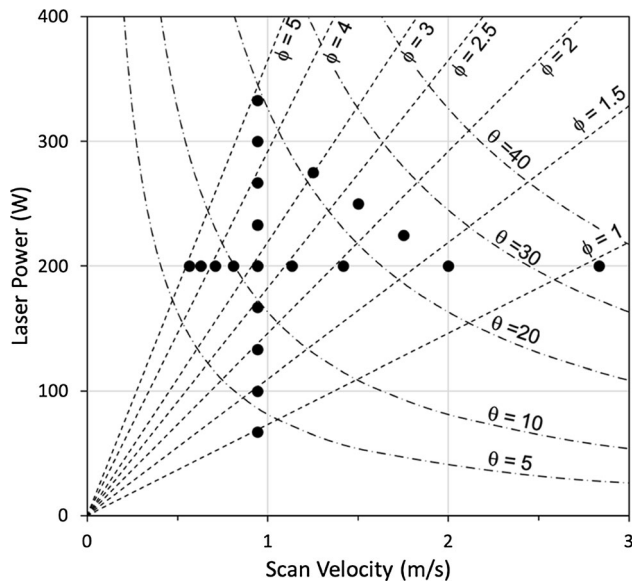


Fig. 3 A map of test builds in P-V space, also showing the ϕ - θ coordinate system (θ given in W/m). Comparisons in Fig. 2 reveal that large-scale porosity correlates directly with ϕ and that builds along constant ϕ lines (solid gray) have similar porosity indicative of similar degree of remelting. The θ parameter, the product of PV/D, is useful for assessing build efficiency since it is generally related inversely to production time.

principal gradient direction for build soundness with respect to melt-fusion, while θ is associated with a direction of vanishing gradient (iso-contours) with respect to this property. The corresponding alternative parameterization grid is superim-

posed on the P-V plot in Fig. 3, showing all test builds. The utility of this parameterization for process-mapping and cross-material comparison will be assessed more generally in a later section.

Another measure of the effects of incomplete melting at this scale is the surface roughness of the build, and measurements of surface roughness (R_A) were taken for double-layer specimens. Corresponding cross-sections are shown in Fig. 4, clearly revealing a strong inverse correlation with ϕ , where the highly irregular surface associated with incomplete melting at low power ratio becomes much smoother at high power ratio, indicative of full melting and wetting. The surface roughness measurements further reveal an influence of θ , where low and high values of θ are clearly distinguishable.

Mechanical property variation within the test-build parameter space was investigated using uniaxial tension, Rockwell hardness, and Vickers microhardness testing. Tension test specimens were machined from cylindrical pillar builds, 12.7 mm (0.5 in) in diameter and 127 mm (5 in) in length. Specimens were machined to have a reduced section of 7.62 mm (0.3 in) in diameter and 38 mm (1.5 in) in length. Tests were performed using a constant crosshead speed of 0.021 mm/s (0.05 in/min). Strain and load were measured using a 25.4 mm (1 inch) gage length extensometer and a 50-kN load cell, respectively. Tension test results are summarized in Fig. 5. Ultimate tensile strength (UTS) and elongation are both observed to increase with ϕ up to a maximum at approximately $\phi = 3.5$, followed by minor decreases with further increases in ϕ . The best combination of strength and ductility is exhibited by the group of specimens with ϕ between 3 and 4, as shown in Fig. 5(c). In Fig. 5(d), a comparison is made between mechanical properties of specimens with similar values of ϕ but different values of θ . Each point plotted in Fig. 5(d) corresponds to a specimen pair, with high and low values of θ . The specimen designators shown on the plot correspond to the designators and parameters listed in Table 2.

Rockwell C-scale hardness (HRC) and Vickers microhardness (VHN) measurements are summarized in Fig. 6(a) and (b), respectively. Figure 6(a) shows HRC results from 9 build samples with 20 measurements on each sample. In Fig. 6(b), the mean of 35 VHN measurements (5 each on the XY and YZ planes and 25 on the XZ plane) for each build is plotted with error bars indicating $+/- 1$ standard deviation. Similar to the UTS measurements, the HRC measurements exhibit a maximum between $\phi = 3$ and $\phi = 4$. The VHN, however, is not observed to vary appreciably with ϕ . The difference between the HRC and VHN measurements indicates the distinction between the bulk and localized nature of the two types of measurements, shedding light on the origin of property variation. Microhardness indentations at individually selected sites generally fall on a single grain or between individual microstructural features. Accordingly, these measurements do not reflect the collective effects of porosity, grain structure, the build-fusion pattern, and related build defects, which are indicated by tension and bulk (HRC) hardness tests.

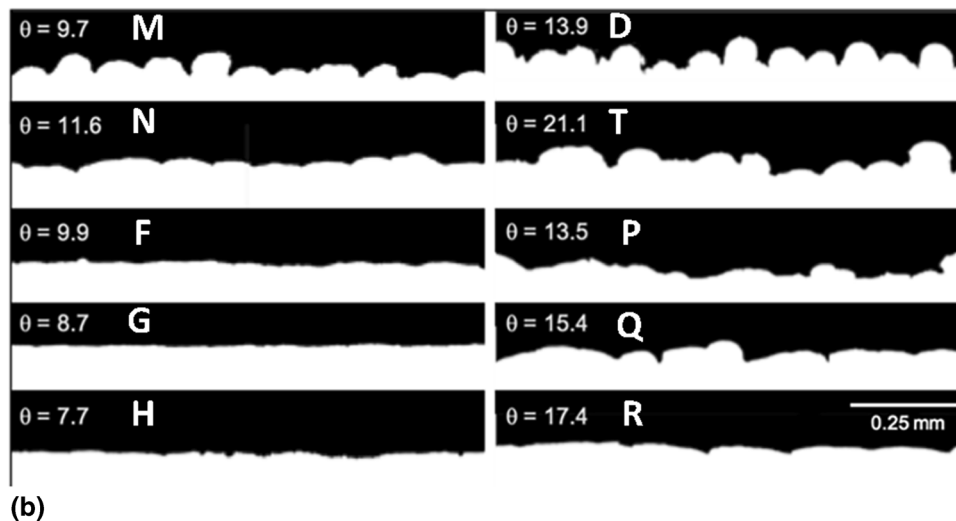
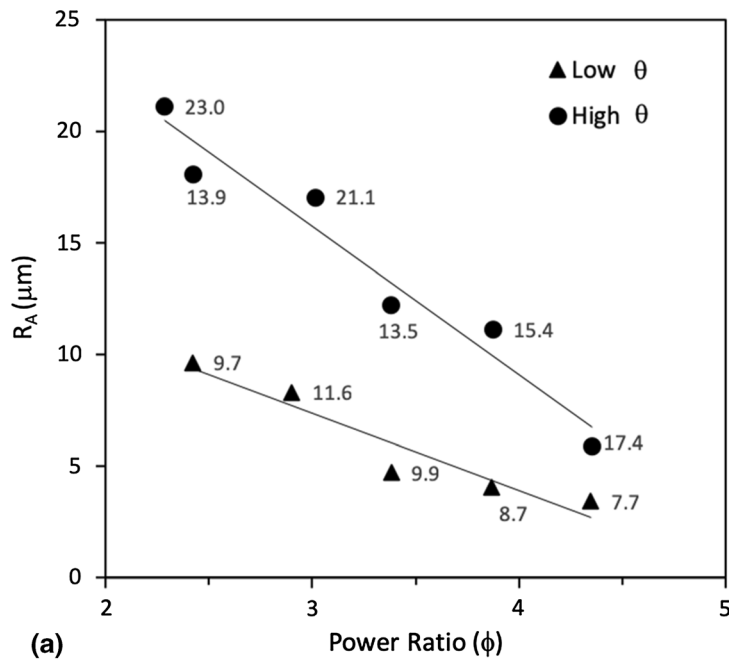


Fig. 4 A summary of the effects of ϕ and θ on the as-built surface of 316L double-layer specimens: (a) surface roughness plotted vs ϕ , showing the corresponding values of θ , (b) corresponding examples of the build surface profiles for the listed values of θ (Build designators correspond to those in Table 2.)

3. Further Analysis and Discussion

The property variation with ϕ , exhibiting maxima in both strength and ductility at approximately $\phi = 3.5$, is an important observation that deserves additional consideration. The increase in UTS and elongation with increasing ϕ are readily understood to be attributed to the increasing degree of melt-fusion, as evidenced by corresponding decreases in gross porosity and surface roughness. While insufficient melting is clearly responsible for lower strength below $\phi \approx 3.5$, the decrease in strength and ductility observed at higher values of ϕ is not so easily

explained. Increased grain size is a likely contributor to the observed decrease in tensile strength (Ref 74, 75). Examining this issue, the grain size was measured for selected specimens with an intercept method using at least 50 circular test patterns and a total test line length of approximately 15 mm. Results are plotted in Fig. 7, revealing two notable features. First, the specimens do indeed exhibit an increase in grain size with increasing ϕ . Second, and perhaps more strikingly, we note that the measurements suggest two distinct regimes of behavior, with a much stronger ϕ dependence above approximately $\phi \approx 3.5$. It is interesting that this transition in grain size dependence occurs at the power ratio above which complete

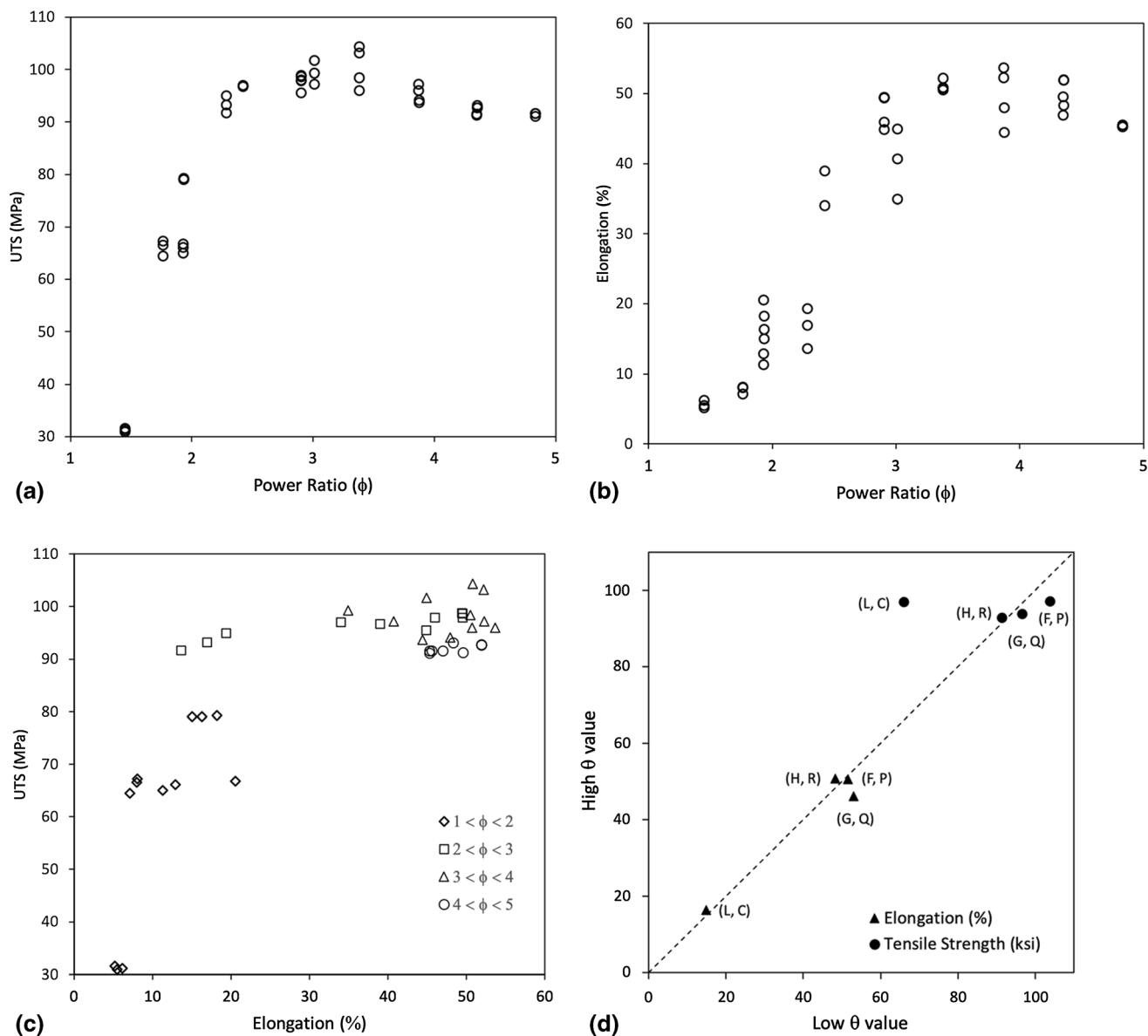
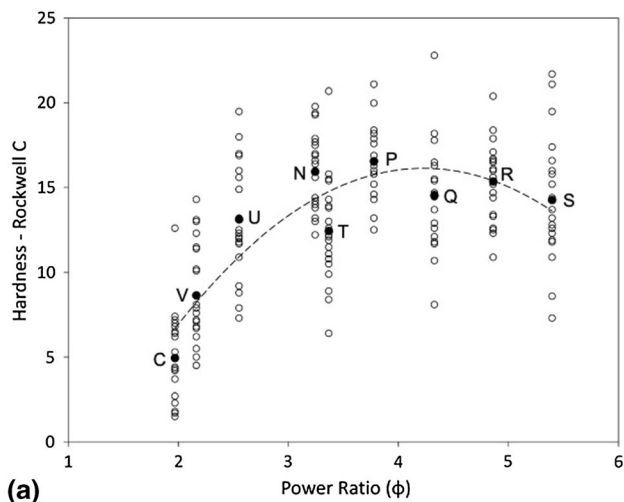


Fig. 5 Tension test results for selected build conditions as a function of power ratio in (a), (b) and direct comparison in (c). d Comparison of the high θ to low θ results showing θ is not by itself an important contributor. (Letters correspond to the specimens in Table 2.)

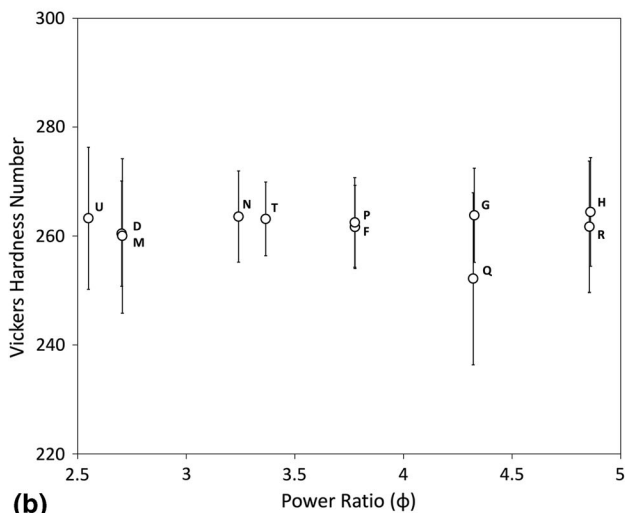
fusion was observed, as indicated by the change from macroporosity to microporosity (Fig. 2), and that for which maximum tensile strength and ductility was generally observed (Fig. 5). The apparent threshold indicates a number of local remelt/reheat cycles (N_{melt}), above which a representative volume element exhibits more extensive grain growth per heating cycle, suggesting a porosity-related grain boundary pinning effect for previous cycles. Whether this threshold is a general phenomenon or a behavior specific to this particular material and geometry remains to be determined. It is expected that this effect would not be observed in multiphase materials where the principal pinning forces arising from precipitates would likely mask the porosity-related pinning effects. In any

event, it is plainly clear that, for 316L, grain size and related properties are strongly correlated with ϕ .

In addition to the direct contribution to mechanical properties associated with grain size, increasing ϕ beyond approximately 3.5 may have a deleterious effect on strength and elongation if higher N_{melt} leads to a larger population of defects that promote mechanical failure. SEM examination of cube-shaped builds reveals that micro-pores and inclusions were observed most frequently along grain boundaries and melt fusion lines (melt-trace boundaries). Typical defect structures are shown in Fig. 8. Investigation of these defects with energy-dispersive spectroscopy (EDS) microchemical analysis identified no correlation with any specific type of chemical segregation or second phase particles, reinforcing the assertion that



(a)



(b)

Fig. 6 (a) Rockwell hardness (HRC), showing individual measurements (open circles) and average values (closed circles); (b) Vickers microhardness (VHN), showing the variation as +/- one standard deviation. (Letters correspond to the specimens in Table 2.)

these fusion-line defects are predominantly micropores. As such, it is reasonable that these become more prevalent at high values of ϕ , where higher melt-pool temperatures may give rise to increased volatilization, gas evolution, and associated fusion-line microporosity (Ref 76). Of course, the relationship between maximum melt-pool temperature and ϕ will depend on the inter-pass dwell time between melting cycles (i.e., the reciprocal of the local trace frequency), as compared with the thermal dissipation rate (i.e., diffusivity). Since the dwell time is a spatially varying local process variable that is dependent on part geometry and scan pattern design, it is beyond the scope of the current analysis. However, an analytical treatment by Ward (Ref 77) has shown that the melt-cycle frequency and the effect of nearby traces may lead to significant preheating before melting. This preheating effect (and its spatial variation) could easily be accounted for by applying the current treatment within a geometric analysis for a given component through the variation of the local ambient temperature, T_A , in Eq 1, reducing the heating requirements and increasing the local value of ϕ .

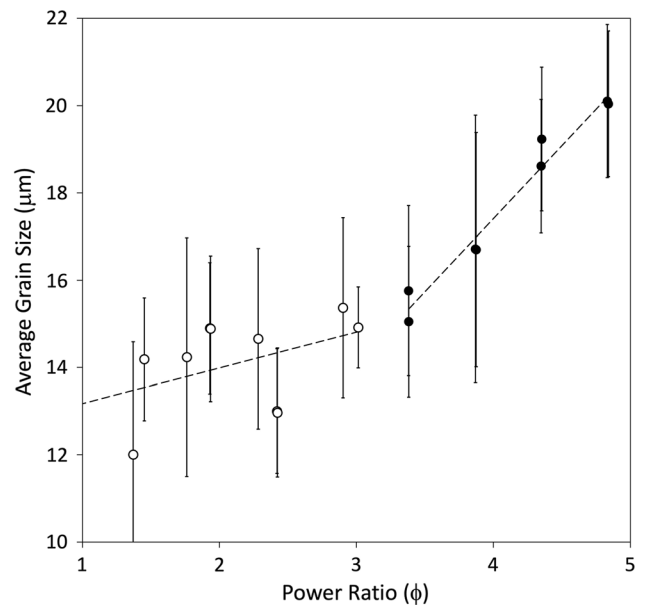


Fig. 7 Grain size measurement results showing two distinct regimes. Grain size was measured with an intercept method using at least 50 circular test patterns and a total test line length of approximately 15 mm. The average standard deviation is 1.88 μm . The dashed lines are linear fits for the two respective data sets, distinguished here as light or dark circles.

With a clear connection between ϕ and the mechanical properties of the build and with associated correlations to grain structure and microstructural defects, it is desirable to relate ϕ to measurable features of the build. Based on single-trace cross sections, like the example shown in Fig. 9a, measurements of depth and width of the laser-melt trace show that these dimensions scale with ϕ (Fig. 9b). Of course, these dimensions are not readily measurable in a bulk build. The radius of curvature at the root of the melt trace, however, is observable in the bulk (Fig. 9c), and our measurements show that it is a reasonable indicator of the other trace dimensions (Fig. 9d) and therefore a good indicator of ϕ . In this manner, the trace root radius provides a means for direct estimation of ϕ in a bulk build, which is strongly correlated with build soundness and mechanical properties, as we have shown.

To this point, the analysis has demonstrated the value of the power ratio parameter, ϕ , as an indicator of melt-intensity, build soundness, and related properties (i.e., strength, ductility, and surface roughness) for 316L stainless steel. As a parameter of general utility, however, it remains to be shown that ϕ can be used for effective cross-material comparison. For this purpose, a comparison of reported parametric investigations for Fe-, Al-, Ni-, and Ti-based alloys is provided in Fig. 10. In this general summary of available data, reported findings related to observed porosity and build soundness and/or mechanical properties are used to classify specific build trials as unacceptable or acceptable, based on descriptions of the respective authors. Figure 10 shows a direct comparison of data in the P-V process parameter space for several types of alloys. Of course, this has limited value for cross-material comparison or the extension of process experience to expected behavior of alternative alloys. In Fig. 11(a), the same sound/unsound data for all four alloy classes are plotted together in ϕ - θ space. In addition, where some sort of optimum condition was reported,

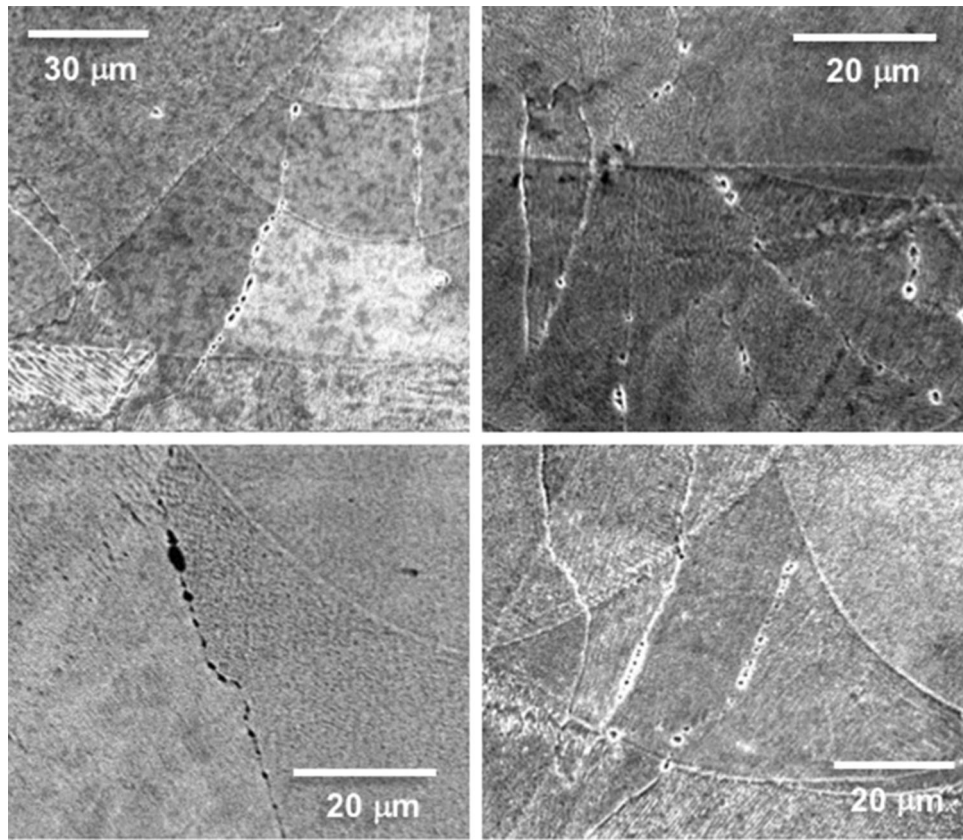


Fig. 8 Examples of typical grain boundary defects that become more frequent above the optimum ($\phi \approx 3.5$), shown here in sample R ($\phi \approx 4.35$) with SEM secondary electron contrast

the corresponding data are labeled as such. This figure highlights the effectiveness of ϕ for cross-material comparison, where the large body of data are seen to suggest common lower and upper limits across the four different alloy types. We interpret these limits as being associated with the effects of insufficient melting and overheating and have included lines to illustrate such limits, approximately 2.5 and 4.5, respectively, based on a simple inspection of the data. To assess the data in more detail, the distribution of data from Fig. 11(a) is plotted in Fig. 11(b) as separate histograms for unsound, sound, and optimum builds, showing peaks at $\phi = 1.3$, 2.8, and 3.3, respectively. Additionally, the optimum and acceptable are combined and compared with unacceptable (unsound) builds, with a peak of $\phi = 3.0$. This simple comparison is consistent with our analysis for 316L, where ϕ in the range of 3–4 produced the best combination of observable build soundness and mechanical properties.

In order to better normalize the rate-dependent effects of localized heating and cooling across the different alloy systems, we define a local heating time,

$$t_h = \frac{d_B \pi}{4v}, \quad (\text{Eq 2})$$

and a thermal dissipation time,

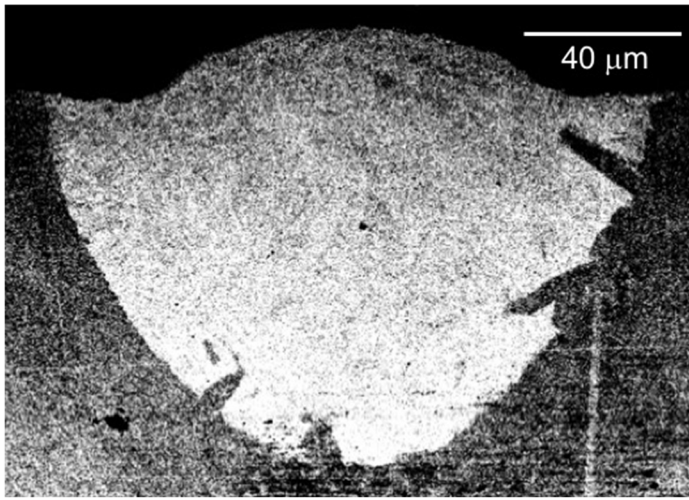
$$t_d = \beta \left(\frac{d_B^2}{D} \right), \quad (\text{Eq 3})$$

where the ratio between the two provides a dimensionless thermal relaxation time,

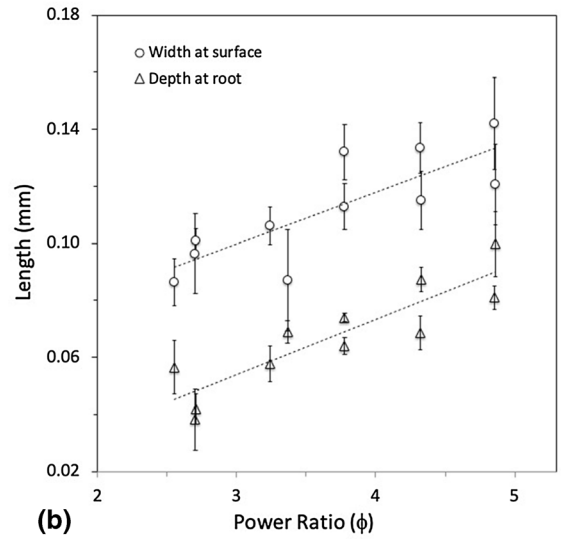
$$\tau \equiv \frac{t_d}{t_h} = \frac{4\beta d_B v}{\pi D} \quad (\text{Eq 4})$$

Here, β is a dimensionless geometric factor associated with the characteristic exponential decay time for the surface temperature following a heating pulse over a circular area. Using a 1-D finite difference model (i.e., spherical symmetry) with a simple hemispherical heat pulse. Starting with the entire volume at 298 K, the pulse is applied by instantaneously raising the temperature within a small hemispherical volume of diameter d_B (i.e., at the free surface) to a fixed temperature (T_p) and computing diffusive thermal relaxation (assuming no dissipation from the surface). With this simple approach, we examined heating pulse diameters ranging from 0.05 to 0.20 mm and thermal diffusivities from 1 to 100 mm²/s and measured the decay time (t_d) as the time required for the center of the heated material on the free surface to decay to a temperature of $T_p e^{-1}$. In this way, we assessed β to be 0.0285, as listed in Table 3.

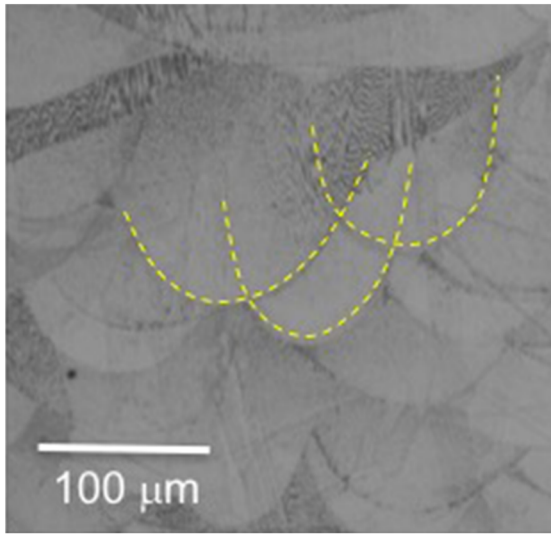
Using τ (Eq. 4) as a characteristic thermal relaxation time, we examine in Fig. 12a the full set of reported data using a $\phi - \tau$ parameter space, suggesting a general cross-material behavior with respect to τ . The distributions for the three build soundness types are shown separately in Fig. 12b. There is not a substantial difference between these distributions, but the distribution frequency plot in the inset does show that the distribution of all builds is heavily populated in the region of $0.5 < \tau < 2$. This is not particularly surprising, indicating that τ is a relevant time scale, with effective upper and lower



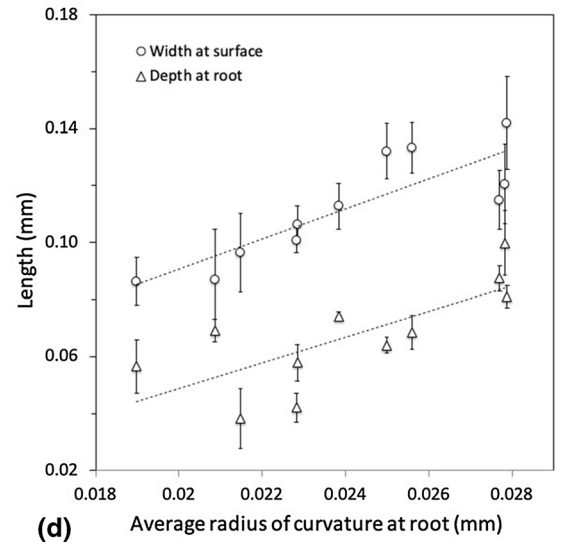
(a)



(b)



(c)



(d)

Fig. 9 Relationship between melt-pool dimensions and the power ratio. **a** Example of a single-trace cross-section and **b** melt-trace dimension measurement results. **c** 3D build cross-sectional example showing root curvature, and **d** correlation with trace dimensions

limits associated with insufficient and excessive heating, respectively. The cursory but broad comparison of reported data shown in Fig. 11 and 12 demonstrates that the $\phi - \tau$ parameter space, indeed, provides a useful platform for cross material comparison and process mapping, and the suggested sound build space (approximately $2.5 < \phi < 4.5$ and $0.5 < \tau < 2.0$) provides a reasonable starting point for process/component design.

4. Conclusion

The bulk SLM fabrication of 316L stainless steel was assessed over a range of process parameters. Through evaluation of melt-pool characteristics, microstructure, defects, and mechanical properties, sound-build parameter limits and optimum conditions were identified. To facilitate a comparative parametric evaluation, the power ratio was introduced to

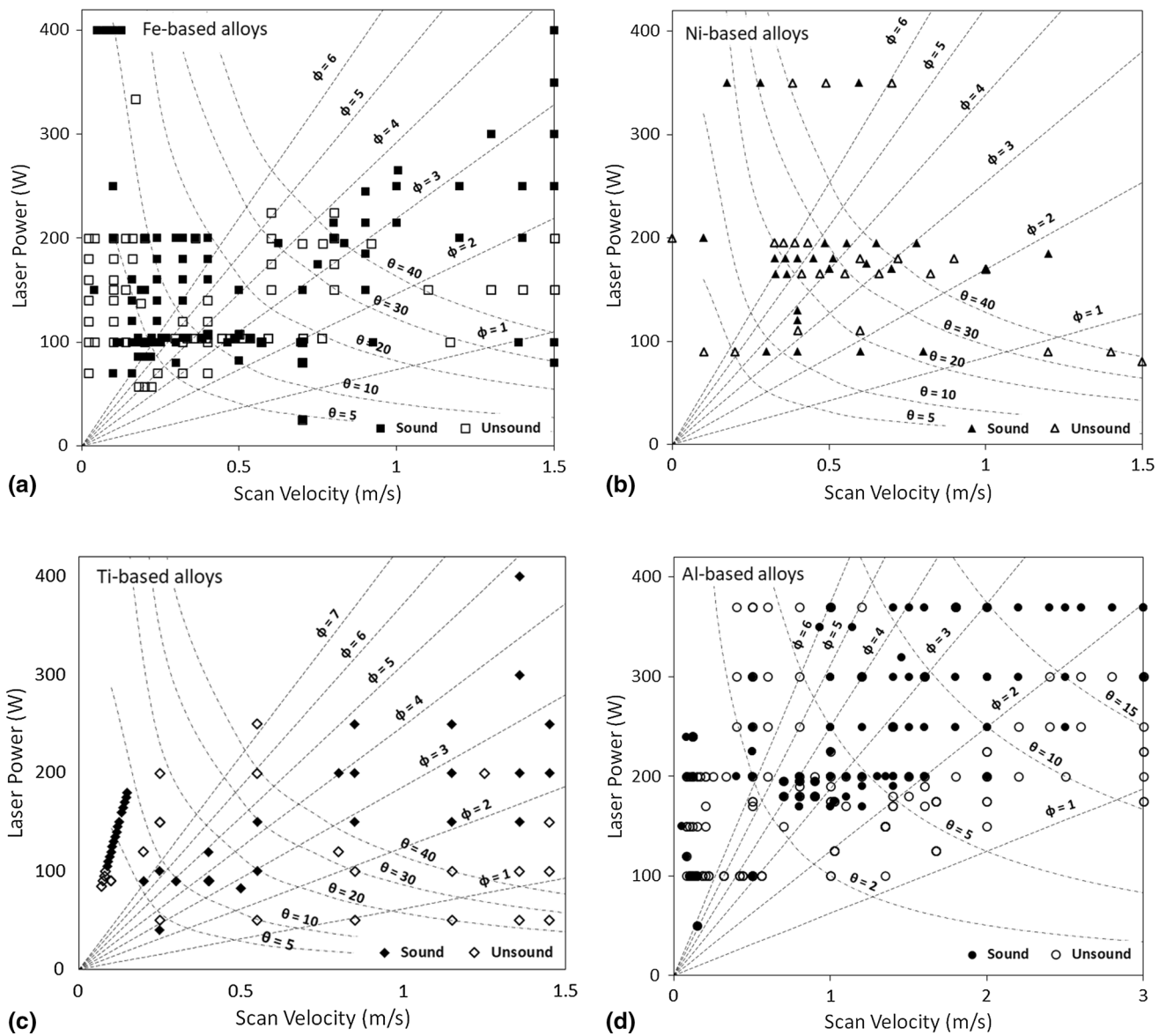


Fig.10 P-V comparison for (a) Fe-based alloys, (b) Ni-based alloys, (c) Ti-based alloys, (d) Al-based alloys. References: [7-12, 12-46], and [47, 48, 50-57]

effectively describe the local melting intensity. Similar to the commonly used energy density, the power ratio accounts for the net laser energy absorbed per unit volume of processed mass. However, using the material-specific heat capacity and latent heat of melting for the material, the power ratio includes the energy required for heating and melting the specific material at the prescribed mass rate. (The parameter may also be used to account for variable non-local preheating effects, but this was not included in the current study.) Indeed, the power ratio is shown to be a principal indicator of melt-fusion-related properties. Furthermore, parametric investigation of 316L indicates that an optimum value of the power ratio exists and that it is approximately 3.5. Lower values of strength and ductility below this optimum are attributed to insufficient melt-

fusion. Property decreases above the optimum power ratio are less pronounced but are attributed to grain growth and increased frequency of fusion line defects, both of which are clearly observed in this study.

Build characteristics were assessed using a parameter space defined by the power ratio, ϕ , and an effective linear power density, θ , which incorporates the rate-dependent thermal dissipation length. Examination of macro-porosity associated with melting indicates that this is a natural parameterization, defining maximum and zero gradient directions for the effective heating intensity. This parameterization was used to compare reported data across various alloy types (Fe-, Ni-, Al-, and Ti-based), showing general applicability with respect to normalized melting behavior, suggesting practical upper and lower

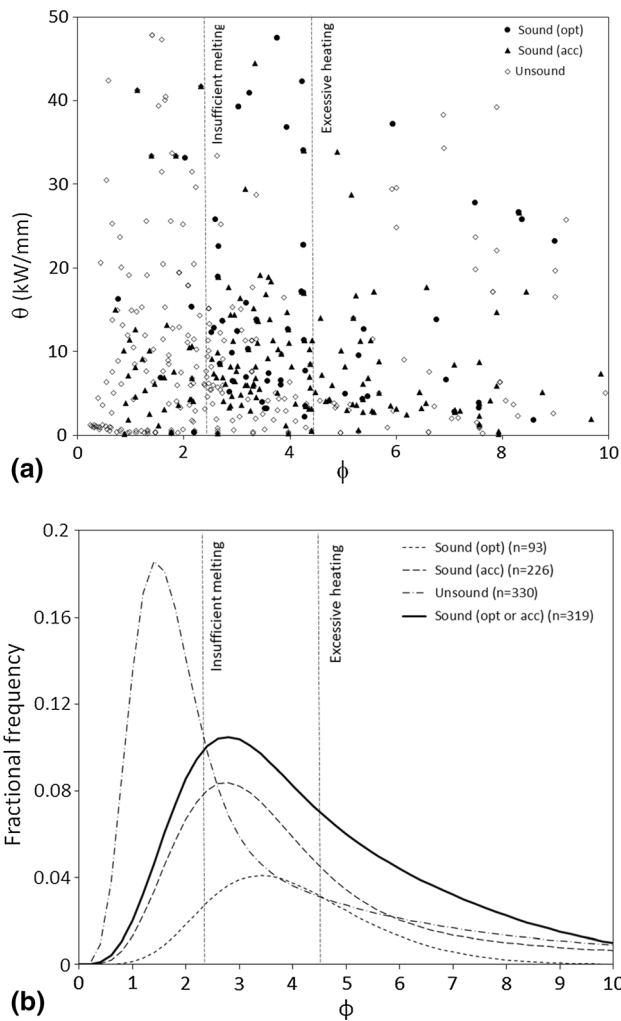


Fig. 11 (a) ϕ - θ space for reported Fe-, Al-, Ni-, and Ti-based alloys. (b) histograms for power ratio, ϕ , for the three types of reported build data shown in (a) (acceptable, unacceptable, and optimum), also highlighting combined histogram for acceptable and optimum. References: [7-12, 12-46], and [47-57]

bounds for ϕ , associated with insufficient melting and excessive heating, respectively. As such, constant- ϕ contours can provide useful processing guidelines that are transferable across materials.

To better characterize the rate dependence, the dimensionless power ratio, ϕ , was also coupled with a dimensionless time, τ , which scales local heating time with the specific characteristic thermal relaxation time. With broad data comparison, the dimensionless ϕ - τ parameterization suggests general (cross-material) upper and lower bounds for sound builds.

The value of the parameterizations introduced here is strongly supported by our investigation including measurements of microstructural features, defects, and mechanical properties, and also by our broad review of reported SLM build studies. Certainly, the utility of these parameterizations for general cross-material comparison over various geometries requires additional investigation. However, the present study and cursory comparison of available reports provide a compelling argument for further consideration.

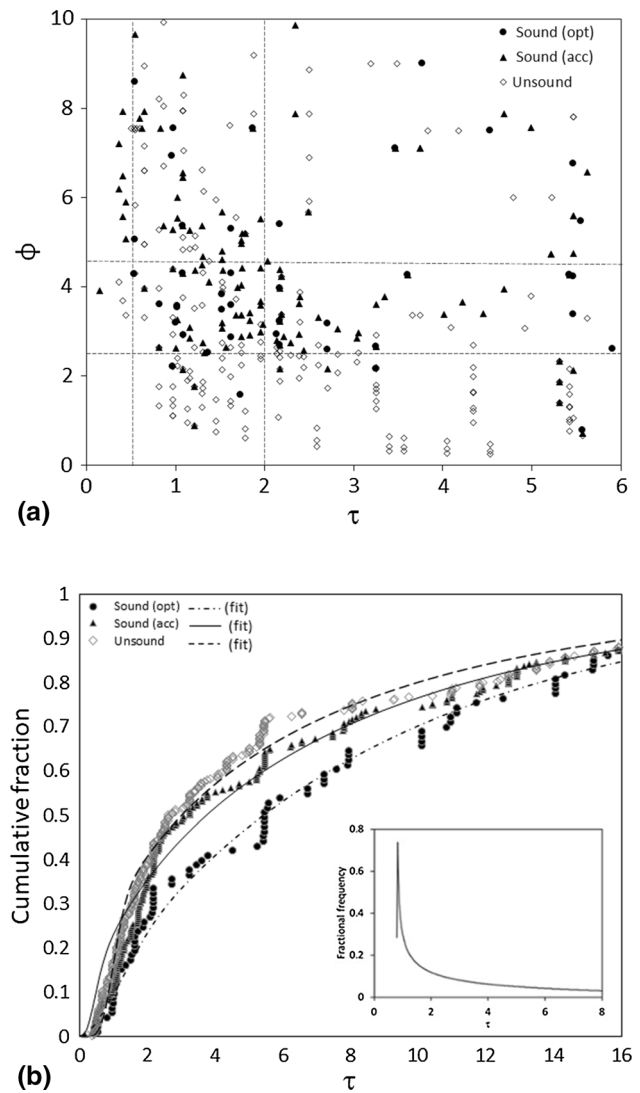


Fig. 12 a ϕ - τ parameter space for reported Fe-, Al-, Ni-, and Ti-based alloys. b Distributions of the dimensionless dissipation time, τ , for the three types of reported build data shown in (a) (unsound, sound, and optimum). References: [7-12, 12-46], and [47-57]

Acknowledgments

This work was supported by Deere and Company, Moline Technology Center, Moline IL, under John Deere contract #407569001. The authors would also like to acknowledge the supporting efforts of David Puente, Tina Berthiaume, Sam Conley, Jeremy Knibbe, Austin Dicus, Tim Matchulat, Ashley McKenna, and Alexandria Springer. Finally, the authors would like to thank Ryan Spotts (Emerson Automation Solutions, Marshalltown, IA) for various technical discussions related to SLM processing.

References

1. W. Gao, Y. Zhang, D. Ramanujan, K. Ramani, Y. Chen, C.B. Williams, C.C.L. Wang, Y.C. Shin, S. Zhang, and P.D. Zavattieri, The Status, Challenges, and Future of Additive Manufacturing in Engineering, *CAD Comput. Aided Des.*, 2015, **69**, p 65–89. <https://doi.org/10.1016/j.cad.2015.04.001>
2. N. Li, S. Huang, G. Zhang, R. Qin, W. Liu, H. Xiong, G. Shi, and J. Blackburn, Progress in Additive Manufacturing on New Materials: A

- Review, *J. Mater. Sci. Technol.*, 2018, **35**, p 242–269. <https://doi.org/10.1016/j.jmst.2018.09.002>
3. M. Ghobakhloo, The Future of Manufacturing Industry: A Strategic Roadmap Toward Industry 4.0, *J. Manuf. Technol. Manag.*, 2018, **29**, p 910–936. <https://doi.org/10.1108/JMTM-02-2018-0057>
 4. S.A.M. Tofail, E.P. Koumoulos, A. Bandyopadhyay, S. Bose, L. O'Donoghue, and C. Charitidis, Additive Manufacturing: Scientific and Technological Challenges, Market Uptake and Opportunities, *Mater. Today*, 2018, **21**, p 22–37. <https://doi.org/10.1016/j.mattod.2017.07.01>
 5. T.D. Ngo, A. Kashani, G. Imbalzano, K.T.Q. Nguyen, and D. Hui, Additive Manufacturing (3D Printing): A Review of Materials, Methods, Applications and Challenges, *Compos. Part B Eng.*, 2018, **143**, p 172–196. <https://doi.org/10.1016/j.compositesb.2018.02.012>
 6. M. Martinsuo and T. Luomaranta, Adopting Additive Manufacturing in Smes: Exploring the Challenges and Solutions, *J. Manuf. Technol. Manag.*, 2018 <https://doi.org/10.1108/JMTM-02-2018-0030>
 7. E. Brandl, U. Heckenberger, V. Holzinger, and D. Buchbinder, Additive Manufactured AlSi10Mg Samples Using Selective Laser Melting (SLM) Microstructure, High Cycle Fatigue, and Fracture Behavior, *Mater. Des.*, 2012, **34**, p 159–169
 8. K. Kempen, L. Thijs, J. Van Humbeeck, and J.P. Kruth, Processing AlSi10Mg by Selective Laser Melting: Parameter Optimisation and Material Characterisation, *Mater. Sci. Technol.*, 2015, **31**, p 917–923. <https://doi.org/10.1179/1743284714Y.0000000702>
 9. S. Rao, K. Yang, X.H. Wu, C.H.J. Davies, and H. Giet, The Influence of Processing Parameters on Aluminium Alloy A357 Manufactured by Selective Laser Melting, *Mater. Des.*, 2016, **109**, p 334–346. <https://doi.org/10.1016/j.matdes.2016.07.009>
 10. R. Noriko, W. Wang, E. Khamis, and M.M. Attallah, Selective Laser Melting of AlSi10Mg Alloy: PROCESS Optimisation and Mechanical Properties Development, *Mater. Des.*, 2015, **65**, p 417–424. <https://doi.org/10.1016/j.matdes.2014.09.044>
 11. S. Siddique, M. Imran, E. Wycisk, C. Emmelmann, and F. Walther, Influence of Process-Induced Microstructure and Imperfections on Mechanical Properties of AlSi12 Processed by Selective Laser Melting, *J. Mater. Process. Technol.*, 2015, **221**, p 205–213. <https://doi.org/10.1016/j.jmatprotec.2015.02.023>
 12. M. Simonelli, C. Tuck, N.T. Aboulkhair, I. Maskery, I. Ashcroft, R.D. Wildman, and R. Hague, A Study on the Laser Spatter and the Oxidation Reactions During Selective Laser Melting of 316L Stainless Steel, Al-Si10-Mg, and Ti-6Al-4V, *Metall. Mater. Trans. a-Physical Metall. Mater. Sci.*, 2015, **46**, p 3842–3851. <https://doi.org/10.1007/s11661-015-2882-8>
 13. Y. Yang, Y. Chen, J.X. Zhang, X.H. Gu, P. Qin, N.W. Dai, X.P. Li, J.P. Kruth, and L.C. Zhang, Improved Corrosion Behavior of Ultrafine-Grained Eutectic Al-12Si Alloy Produced by Selective Laser Melting, *Mater. Des.*, 2018, **146**, p 239–248. <https://doi.org/10.1016/j.matdes.2018.03.025>
 14. H. Zhang, H. Zhu, X. Nie, J. Yin, Z. Hu, and X. Zeng, Effect of Zirconium Addition on Crack, Microstructure and Mechanical Behavior of Selective Laser Melted Al-Cu-Mg Alloy, *Scr. Mater.*, 2017, **134**, p 6–10
 15. T. Kimura and T. Nakamoto, Microstructures and Mechanical Properties of A356 (AlSi7Mg0.3) Aluminum Alloy Fabricated by Selective Laser Melting, *Mater. Des.*, 2016, **89**, p 1294–1301. <https://doi.org/10.1016/j.matdes.2015.10.065>
 16. M. Krishnan, E. Atzeni, R. Canali, F. Calignano, D. Manfredi, E.P. Ambrosio, and L. Iuliano, On the Effect of Process Parameters on Properties of AlSi10Mg Parts Produced by DMLS, *Rapid Prototyp. J.*, 2014, **20**, p 449–458. <https://doi.org/10.1108/Rpjt-03-2013-0028>
 17. W. Li, S. Li, J. Liu, A. Zhang, Y. Zhou, Q. Wei, C. Yan, and Y. Shi, Effect of Heat Treatment on AlSi10Mg Alloy Fabricated by Selective Laser Melting: Microstructure Evolution, Mechanical Properties and Fracture Mechanism, *Mater. Sci. Eng. A.*, 2016, **663**, p 116–125. <https://doi.org/10.1016/j.msea.2016.03.088>
 18. X.P. Li, K.M. O'Donnell, and T.B. Sercombe, Selective Laser Melting of Al-12Si Alloy: Enhanced Densification via Powder Drying, *Addit. Manuf.*, 2016, **10**, p 10–14. <https://doi.org/10.1016/j.addma.2016.01.003>
 19. E.O. Olakanmi, Selective Laser Sintering/Melting (SLS/SLM) of Pure Al, Al-Mg, and Al-Si Powders: Effect of Processing Conditions and Powder Properties, *J. Mater. Process. Technol.*, 2013, **213**, p 1387–1405. <https://doi.org/10.1016/j.jmatprotec.2013.03.009>
 20. E.O. Olakanmi, R.F. Cochrane, and K.W. Dalgarno, A Review on Selective Laser Sintering/Melting (sls/slm) of Aluminium Alloy Powders: Processing, Microstructure, and Properties, *Prog. Mater. Sci.*, 2015, **74**, p 401–477. <https://doi.org/10.1016/j.pmatsci.2015.03.002>
 21. E.O. Olakanmi, R.F. Cochrane, and K.W. Dalgarno, Densification Mechanism and Microstructural Evolution in Selective Laser Sintering of Al-12Si Powders, *J. Mater. Process. Technol.*, 2011, **211**, p 113–121. <https://doi.org/10.1016/j.jmatprotec.2010.09.003>
 22. K.G. Prashanth, S. Scudino, H.J. Klauß, K.B. Surreddi, L. Löber, Z. Wang, A.K. Chaubey, U. Kühn, and J. Eckert, Microstructure and Mechanical Properties of Al-12si Produced by Selective Laser Melting: Effect of Heat Treatment, *Mater. Sci. Eng. A.*, 2014, **590**, p 153–160. <https://doi.org/10.1016/j.msea.2013.10.023>
 23. K. Antony, N. Arivazhagan, and K. Senthilkumaran, Numerical and Experimental Investigations on Laser Melting of Stainless Steel 316L Metal Powders, *J. Manuf. Process.*, 2014, **16**, p 345–355. <https://doi.org/10.1016/j.jmapro.2014.04.001>
 24. J. Liu, Y. Song, C. Chen, X. Wang, H. Li, C. Zhou, J. Wang, K. Guo, and J. Sun, Effect of Scanning Speed on the Microstructure and Mechanical Behavior of 316L Stainless Steel Fabricated by Selective Laser Melting, *Mater. Des.*, 2020, **186**, p 108355. <https://doi.org/10.1016/j.matdes.2019.108355>
 25. E. Liverani, S. Toschi, L. Ceschini, and A. Fortunato, Effect of Selective Laser Melting (SLM) Process Parameters on Microstructure and Mechanical Properties of 316L Austenitic Stainless Steel, *J. Mater. Process. Technol.*, 2017, **249**, p 255–263. <https://doi.org/10.1016/j.jmatprotec.2017.05.042>
 26. P. Murkute, S. Pasebani, and O.B. Isgor, Production of Corrosion-Resistant 316L Stainless Steel Clads on Carbon Steel Using Powder Bed Fusion-Selective Laser Melting, *J. Mater. Process. Technol.*, 2019, **273**, p 116243. <https://doi.org/10.1016/j.jmatprotec.2019.05.024>
 27. W. Shi, P. Wang, Y. Liu, Y. Hou, and G. Han, Properties of 316L Formed by a 400 W Power Laser Selective Laser Melting with 250 µm Layer Thickness, *Powder Technol.*, 2020, **360**, p 151–164. <https://doi.org/10.1016/j.powtec.2019.09.059>
 28. A.B. Spierings, N. Herres, and G. Levy, Influence of the Particle Size Distribution on Surface Quality and Mechanical Properties in AM Steel Parts, *Rapid Prototyp. J.*, 2011, **17**, p 195–202. <https://doi.org/10.1108/13552541111124770>
 29. T. Zhong, K. He, H. Li, and L. Yang, Mechanical Properties of Lightweight 316L Stainless Steel Lattice Structures Fabricated by Selective Laser Melting, *Mater. Des.*, 2019, **181**, p 108076. <https://doi.org/10.1016/j.matdes.2019.108076>
 30. G. Casalino, S.L. Campanelli, N. Contuzzi, and A.D. Ludovico, Experimental Investigation and Statistical Optimisation of the Selective Laser Melting Process of a Maraging Steel, *Opt. Laser Technol.*, 2015, **65**, p 151–158. <https://doi.org/10.1016/j.optlastec.2014.07.021>
 31. J. Delgado, J. Ciurana, and C.A. Rodríguez, Influence of Process Parameters on Part Quality and Mechanical Properties for DMLS and SLM with iron-Based Materials, *Int. J. Adv. Manuf. Technol.*, 2012, **60**, p 601–610. <https://doi.org/10.1007/s00170-011-3643-5>
 32. J.J.S.S. Dilip, G.D.J.J. Ram, T.L. Starr, and B. Stucker, Selective Laser Melting of HY100 Steel: Process Parameters, Microstructure and Mechanical Properties, *Addit. Manuf.*, 2017, **13**, p 49–60. <https://doi.org/10.1016/j.addma.2016.11.003>
 33. M. Huang, Z. Zhang, and P. Chen, Effect of Selective Laser Melting Process Parameters on Microstructure and Mechanical Properties of 316L Stainless Steel Helical Micro-Diameter Spring, *Int. J. Adv. Manuf. Technol.*, 2019, **104**, p 2117–2131. <https://doi.org/10.1007/s0170-019-03928-3>
 34. C. Kamath, B. El-Dasher, G.F. Gallegos, W.E. King, and A. Sisto, Density of Additively-Manufactured, 316L SS Parts Using Laser Powder-Bed Fusion at Powers up to 400 W, *Int. J. Adv. Manuf. Technol.*, 2014, **74**, p 65–78. <https://doi.org/10.1007/s00170-014-5954-9>
 35. W.E. King, H.D. Barth, V.M. Castillo, G.F. Gallegos, J.W. Gibbs, D.E. Hahn, C. Kamath, and A.M. Rubenchik, Observation of Keyhole-Mode Laser Melting in Laser Powder-Bed Fusion Additive Manufacturing, *J. Mater. Process. Technol.*, 2014, **214**, p 2915–2925. <https://doi.org/10.1016/j.jmatprotec.2014.06.005>
 36. J.P. Kruth, L. Froyen, J. Van Vaerenbergh, P. Mercelis, M. Rombouts, and B. Lauwers, Selective Laser Melting of Iron-Based Powder, *J. Mater. Process. Technol.*, 2004, **149**, p 616–622. <https://doi.org/10.1016/j.jmatprotec.2003.11.051>

37. T. Larimian, M. Kannan, D. Grzesiak, B. AlMangour, and T. Borkar, Effect of Energy Density and Scanning Strategy on Densification, Microstructure and Mechanical Properties of 316L Stainless Steel Processed via Selective Laser Melting, *Mater. Sci. Eng. A.*, 2020, **770**, p 138455. <https://doi.org/10.1016/j.msea.2019.138455>
38. M. Amirjan and H. Sakiani, Effect of Scanning Strategy and Speed on the Microstructure and Mechanical Properties of Selective Laser Melted IN718 Nickel-Based Superalloy, *Int. J. Adv. Manuf. Technol.*, 2019, **103**, p 1769–1780. <https://doi.org/10.1007/s00170-019-03545-0>
39. J.P. Choi, G.H. Shin, S. Yang, D.Y. Yang, J.S. Lee, M. Brochu, and J.H. Yu, Densification and Microstructural Investigation of Inconel 718 Parts Fabricated by Selective Laser Melting, *Powder Technol.*, 2017, **310**, p 60–66. <https://doi.org/10.1016/j.powtec.2017.01.030>
40. V.D. Divya, R. Munoz-Moreno, O. Messe, J.S. Barnard, S. Baker, T. Illston, and H.J. Stone, Microstructure of Selective Laser Melted CM247LC Nickel-Based Superalloy and its Evolution Through Heat Treatment, *Mater. Charact.*, 2016, **114**, p 62–74. <https://doi.org/10.1016/j.matchar.2016.02.004>
41. N.J. Harrison, I. Todd, and K. Mumtaz, Reduction of Micro-Cracking in Nickel Superalloys Processed by Selective Laser Melting: A Fundamental Alloy Design Approach, *Acta Mater.*, 2015, **94**, p 59–68. <https://doi.org/10.1016/j.actamat.2015.04.035>
42. Q.B. Jia and D.D. Gu, Selective Laser Melting Additive Manufacturing of Inconel 718 Superalloy Parts: Densification, Microstructure and Properties, *J. Alloys Compd.*, 2014, **585**, p 713–721. <https://doi.org/10.1016/j.jallcom.2013.09.171>
43. C. Li, R. White, X.Y. Fang, M. Weaver, and Y.B. Guo, Microstructure Evolution Characteristics of Inconel 625 Alloy from Selective Laser Melting to Heat Treatment, *Mater. Sci. Eng. A.*, 2017, **705**, p 20–31. <https://doi.org/10.1016/j.msea.2017.08.058>
44. L.M. Sochalski-Kolbus, E.A. Payzant, P.A. Cornwell, T.R. Watkins, S.S. Babu, R.R. Dehoff, M. Lorenz, O. Ovchinnikova, and C. Duty, Comparison of Residual Stresses in Inconel 718 Simple Parts Made by Electron Beam Melting and Direct Laser Metal Sintering (vol 46A, pg 1419, 2015), *Metall. Mater. Trans. a-Physical Metall. Mater. Sci.*, 2015, **46A**, p 2322. <https://doi.org/10.1007/s11661-015-2810-y>
45. T. Vilaro, C. Colin, J.D. Bartout, L. Naze, and M. Sennour, Microstructural and mechanical approaches of the selective laser melting process applied to a nickel-base superalloy, *Mater. Sci. Eng. a-Structural Mater. Prop. Microstruct. Process.*, 2012, **534**, p 446–451. <https://doi.org/10.1016/j.msea.2011.11.092>
46. C.Y. Yap, H.K. Tan, Z. Du, C.K. Chua, and Z. Dong, Selective Laser Melting of Nickel Powder, *Rapid Prototyp. J.*, 2017, **23**, p 750–757. <https://doi.org/10.1108/RPJ-01-2016-0006>
47. M. Naveed Ahsan, A.J. Pinkerton, R.J. Moat, and J. Shackleton, A comparative study of laser direct metal deposition characteristics using gas and plasma-atomized Ti-6Al-4V powders, *Mater. Sci. Eng. A.*, 2011, **528**, p 7648–7657
48. H. Ali, H. Ghadbeigi, and K. Mumtaz, Effect of Scanning Strategies on Residual Stress and Mechanical Properties of Selective Laser Melted Ti6Al4V, *Mater. Sci. Eng. A.*, 2018, **712**, p 175–187. <https://doi.org/10.1016/j.msea.2017.11.103>
49. D.K. Do and P. Li, The Effect of Laser Energy Input on the Microstructure, Physical and Mechanical Properties of Ti-6Al-4V alloys by Selective Laser Melting, *Virtual Phys. Prototyp.*, 2016, **11**, p 41–47. <https://doi.org/10.1080/17452759.2016.1142215>
50. H. Attar, M. Calin, L.C. Zhang, S. Scudino, and J. Eckert, Manufacture by Selective Laser Melting and Mechanical Behavior of Commercially Pure Titanium, *Mater. Sci. Eng. a-Structural Mater. Prop. Microstruct. Process.*, 2014, **593**, p 170–177. <https://doi.org/10.1016/j.msea.2013.11.038>
51. N.W. Dai, L.C. Zhang, J.X. Zhang, Q.M. Chen, and M.L. Wu, Corrosion Behavior of Selective Laser Melted Ti-6Al-4V Alloy in NaCl Solution, *Corros. Sci.*, 2016, **102**, p 484–489. <https://doi.org/10.1016/j.corsci.2015.10.041>
52. D.D. Gu, Y.C. Hagedorn, W. Meiners, G.B. Meng, R.J.S. Batista, K. Wissenbach, and R. Poprawe, Densification Behavior, Microstructure Evolution, and Wear Performance of Selective Laser Melting Processed Commercially Pure Titanium, *Acta Mater.*, 2012, **60**, p 3849–3860. <https://doi.org/10.1016/j.actamat.2012.04.006>
53. R. Konečná, L. Kunz, A. Bača, and G. Nicoletto, Resistance of Direct Metal Laser Sintered Ti6Al4V Alloy Against Growth of Fatigue Cracks, *Eng. Fract. Mech.*, 2017, **185**, p 82–91. <https://doi.org/10.1016/j.engfracmech.2017.03.033>
54. L. Parry, I.A. Ashcroft, and R.D. Wildman, Understanding the Effect of Laser Scan Strategy on Residual Stress in Selective Laser Melting Through Thermo-Mechanical Simulation, *Addit. Manuf.*, 2016, **12**, p 1–15. <https://doi.org/10.1016/j.addma.2016.05.014>
55. P. Promopattum, R. Onler, and S.-C. Yao, Numerical and Experimental Investigations of Micro and Macro Characteristics of Direct Metal Laser Sintered Ti-6Al-4V Products, *J. Mater. Process. Technol.*, 2017, **240**, p 262–273. <https://doi.org/10.1016/j.jmatprotec.2016.10.005>
56. B. Vrancken, L. Thijs, J.P. Kruth, and J. Van Humbeeck, Heat Treatment of Ti6Al4V Produced by Selective Laser Melting: Microstructure and Mechanical Properties, *J. Alloys Compd.*, 2012, **541**, p 177–185. <https://doi.org/10.1016/j.jallcom.2012.07.022>
57. Z. Wang, Z. Xiao, Y. Tse, C. Huang, and W. Zhang, Optimization of Processing Parameters and Establishment of a Relationship Between Microstructure and Mechanical Properties of SLM Titanium Alloy, *Opt. Laser Technol.*, 2019, **112**, p 159–167. <https://doi.org/10.1016/j.optlastec.2018.11.014>
58. U. Scipioni Bertoli, A.J. Wolfer, M.J. Matthews, J.P.R. Delplanque, and J.M. Schoenung, On the Limitations of Volumetric Energy Density as a Design Parameter for Selective Laser Melting, *Mater. Des.*, 2017, **113**, p 331–340. <https://doi.org/10.1016/j.matdes.2016.10.037>
59. K.G. Prashanth, S. Scudino, T. Maity, J. Das, and J. Eckert, Is the Energy Density a Reliable Parameter for Materials Synthesis by Selective Laser Melting?, *Mater. Res. Lett.*, 2017, **5**, p 386–390. <https://doi.org/10.1080/21663831.2017.1299808>
60. I. Yadroitsev, A. Gusarov, I. Yadroitsava, and I. Smurov, Single Track Formation in Selective Laser Melting of Metal Powders, *J. Mater. Process. Technol.*, 2010, **210**(12), p 1624–1631. <https://doi.org/10.1016/j.jmatprotec.2010.05.010>
61. S.L. Campanelli, G. Casalino, N. Contuzzi, A. Angelastro, and A.D. Ludovico, Analysis of the Molten/Solidified Zone in Selective Laser Melted Parts, High-Power Laser Mater, *Process. Lasers Beam Deliv. Diagn. Appl III*, 2014, **8963**, p 896311. <https://doi.org/10.1117/12.2042170>
62. D. Rosenthal, Mathematical Theory of Heat Distribution During Welding and Cutting, *Weld. J.*, 1941, **20**, p 220–234
63. M. Tang, P.C. Pistorius, and J.L. Beuth, Prediction of Lack-of-Fusion Porosity for Powder Bed Fusion, *Addit. Manuf.*, 2017, **14**, p 39–48. <https://doi.org/10.1016/j.addma.2016.12.001>
64. P. Promopattum, S.C. Yao, P.C. Pistorius, and A.D. Rollett, A Comprehensive Comparison of the Analytical and Numerical Prediction of the Thermal History and Solidification Microstructure of Inconel 718 Products Made by Laser Powder-Bed Fusion, *Engineering*, 2017, **3**, p 685–694. <https://doi.org/10.1016/J.ENG.2017.05.023>
65. J. Irwin, E.W. Reutzel, P. Michaleris, J. Keist, and A.R. Nassar, Predicting Microstructure From Thermal History During Additive Manufacturing for Ti-6Al-4V, *J. Manuf. Sci. Eng.*, 2016, **138**(11), 111007. <https://doi.org/10.1115/1.4033525>
66. B. Zhang, L. Dembinski, and C. Coddet, The Study of the Laser Parameters and Environment Variables Effect on Mechanical Properties of High Compact Parts Elaborated by Selective Laser Melting 316L Powder, *Mater. Sci. Eng. A.*, 2013, **584**, p 21–31. <https://doi.org/10.1016/j.msea.2013.06.055>
67. I. Tolosa, F. Garciandia, F. Zubiri, F. Zapirain, and A. Esnaola, Study of Mechanical Properties of AISI 316 Stainless Steel Processed by “Selective Laser Melting”, Following Different Manufacturing Strategies, *Int. J. Adv. Manuf. Technol.*, 2010, **51**, p 639–647. <https://doi.org/10.1007/s00170-010-2631-5>
68. Y. Liu, Y. Yang, S. Mai, D. Wang, and C. Song, Investigation into Spatter Behavior During Selective Laser Melting of AISI 316L Stainless steel Powder, *Mater. Des.*, 2015, **87**, p 797–806. <https://doi.org/10.1016/j.matdes.2015.08.086>
69. R. Li, Y. Shi, Z. Wang, L. Wang, J. Liu, and W. Jiang, Densification Behavior of Gas and Water Atomized 316L Stainless Steel Powder During Selective Laser Melting, *Appl. Surf. Sci.*, 2010, **256**(13), p 4350–4356. <https://doi.org/10.1016/j.apsusc.2010.02.030>
70. R. Li, J. Liu, Y. Shi, M. Du, and Z. Xie, 316L Stainless Steel with Gradient Porosity Fabricated by Selective Laser Melting, *J. Mater. Eng. Perform.*, 2010, **19**, p 666–671. <https://doi.org/10.1007/s11665-009-9535-2>
71. S.A. Khairallah and A. Anderson, Mesoscopic Simulation Model of Selective Laser Melting of Stainless Steel Powder, *J. Mater. Process. Technol.*, 2014, **214**, p 2627–2636. <https://doi.org/10.1016/j.jmatprotec.2014.06.001>

72. D. Gu and Y. Shen, Balling Phenomena in Direct Laser Sintering of Stainless Steel Powder: Metallurgical Mechanisms and Control Methods, *Mater. Des.*, 2009, **30**(8), p 2903–2910. <https://doi.org/10.1016/j.matdes.2009.01.013>
73. H. Gu, H. Gong, D. Pal, K. Rafi, T. Starr, and B. Stucker, Influences of Energy Density on Porosity and Microstructure of Selective Laser Melted 17-4PH Stainless Steel, *24th International SFF Symposium - An Additive Manufacturing Conference, SFF2013*, University of Texas at Austin (freeform), p 474–489
74. J. Strößner, M. Terock, and U. Glatzel, Mechanical and Microstructural Investigation of Nickel-Based Superalloy IN718 Manufactured by Selective Laser Melting (SLM), *Adv. Eng. Mater.*, 2015, **17**(8), p 1099–1105. <https://doi.org/10.1002/adem.201500158>
75. J. Tong, C.R. Bowen, J. Persson, and A. Plummer, Mechanical Properties of Titanium-Based Ti–6Al–4V Alloys Manufactured by Powder Bed Additive Manufacture, *Mater. Sci. Technol. (United Kingdom)*, 2017, **33**(2), p 138–148. <https://doi.org/10.1080/02670836.2016.1172787>
76. H. Zhao and T. DebRoy, Pore Formation During Laser Beam Welding of Die-Cast Magnesium Alloy AM60B - Mechanism and Remedy, *Weld. J.*, 2001, **80**(8), p 204s–210s
77. R. Ward, R. Mogrelia, R. Jennings, and M. Attallah, Scan Pattern and Energy Density Effects during Additive Manufacturing, *Program Highlights Additive Manufacturing*, MS&T18 Plenary Session, 2018

Publisher's Note Springer Nature remains neutral with regard to jurisdictional claims in published maps and institutional affiliations.